This is a peer-reviewed, accepted author manuscript of the following research article: Nicolson, E, Lines, D, Mohseni, E & MacLeod, CN 2024, 'Single-bit reception with coded excitation for lightweight advanced ultrasonic imaging systems', IEEE Transactions on Ultrasonics, Ferroelectrics, and Frequency Control. https://doi.org/10.1109/TUFFC.2024.3399743

Single-Bit Reception with Coded Excitation for Lightweight Advanced Ultrasonic Imaging Systems

Ewan Nicolson, David Lines, Ehsan Mohseni and Charles N. MacLeod

***Abstract*— The demand for an efficient and reliable ultrasonic phased array imaging system is not unique to a single industry. Today's imaging systems can be enhanced in a number of areas including; improving scanning and processing times, reducing data storage requirements, simplifying hardware and prolonging probe lifespan. In this work, it is shown that by combining the use of Coded Excitation with single-bit data capture, a number of these areas can be improved. Despite using single-bit receive data, resolution can be recovered through the coded excitation pulse compression process, and shown to produce high Signal-to-Noise Ratio (SNR) images of Phase Coherence Imaging (PCI) and Total Focusing Method (TFM) of tip diffraction in a carbon steel sample. Comparison with conventional single-cycle transmission pulses has shown that little imaging performance degradation is seen despite a significant reduction in data resolution and size. This has also been shown to be effective at low excitation voltages with gain compensation due to the obsolescence of signal saturation concerns when considering single-bit receive data. The ability to compute high-resolution ultrasonic images from low-resolution input data at low transmission voltages has important implications for data compression, acquisition & imaging performance, operator safety and hardware simplification for ultrasonic imaging systems across industrial and medical fields.**

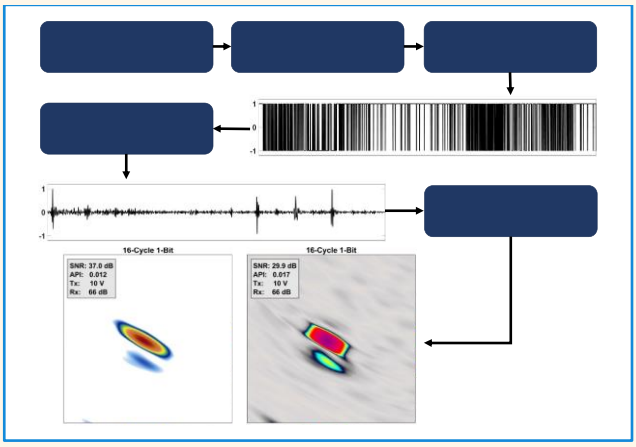

***Index Terms*—Coded Excitation, Phase Coherence imaging, Total Focusing Method, Phased Array, Ultrasonics**

I. Introduction

The ability to determine the internal features and integrity of a subject non-destructively is a crucial process across countless industrial and medical industries. A number of methods are widely used and available, each providing unique advantages for specific applications.

The increasing use of Phased Array Ultrasonic Testing (PAUT) technology has significantly widened the capability of ultrasonic inspection [1]. Contrary to traditional single-element inspection, active beamforming is possible through the electrical excitation of multiple piezoelectric elements with relevant time delays. Focused ultrasound and electronic scanning made possible by this technology have enhanced both the quality of ultrasound inspection, as well as reducing scanning times and dependency on operator interpretation [2].

Additionally, the development of advanced post-processing techniques has been made possible by Full Matrix Capture (FMC) acquisition, allowing the acquisition of a complete ultrasonic dataset for offline synthetic beamforming [3]. Numerous image reconstruction algorithms have been developed for post-processing of FMC data, such as the Total Focusing Method (TFM) [4, 5], Phase Coherence Imaging (PCI) [6], Inverse Wavefield Extrapolation (IWEX) [7] and wavenumber algorithm [8]. The 'gold standard' of these algorithms is TFM, which has demonstrated enhanced image resolution and Signal-to-Noise Ratio (SNR) performance due to the ability to conduct synthetic full-aperture focusing at every image pixel. Developments of TFM, including multi-mode imaging [9] and Vector TFM (VTFM) [10], have built upon the effectiveness of the original algorithm. PCI has gained recent traction within Non-Destructive Testing (NDT) research fields, initially as an enhancement to TFM [6, 11], but also as a stand-alone amplitude-free alternative with the potential to enhance detection and characterisation of diffuse

Submitted on 8th January 2024. This is work is supported by Grant EP/S023275/1.

Ewan Nicolson is with the University of Strathclyde, Glasgow, UK (email: ewan.nicolson@strath.ac.uk).

David Lines is with the University of Strathclyde, Glasgow, UK (email: david.lines@strath.ac.uk).

Ehsan Mohseni is with the University of Strathclyde, Glasgow, UK (email: ehsan.mohseni@strath.ac.uk).

Charles N. Macleod is with the University of Strathclyde, Glasgow, UK (email: charles.macleod@strath.ac.uk).

Highlights

- **Coded Excitation combined with Single-Bit Phase Coherence Imaging has the potential to enable a new and efficient imaging system for data transfer, processing and storage, with little compromise to image quality.**
- **Imaging of tip-diffraction in a carbon steel sample has shown the ability to recover resolution from single-bit receive data using Golay coded excitation to produce high-SNR PCI and TFM images.**
- **This has important implications for data compression, acquisition & imaging performance, operator safety and hardware simplification for ultrasonic imaging systems across industrial and medical fields.**

discontinuities. This has been shown to be particularly beneficial for crack tip detection, due to improved sensitivity to diffractive scatterers [12, 13].

Despite the advantages observed by post-FMC imaging techniques, a key issue must be addressed when considering real-world applications. The NDT process can be performed at various stages of a component's lifecycle – from in-process inspection during heavy pipe welding [14, 15], to resin monitoring during epoxy curing in composite materials [16]. This is vital for critical components in nuclear, petrochemical and renewable fields, with inspections performed regularly to ensure component integrity, and requiring the streaming and real-time processing of large datasets. This can be costly in terms of both the hardware and computational power required to generate images in real-time. Additionally, inspection data is often required to be retained for several decades to allow for lifetime monitoring and analysis of structural health. It is often impractical to store such large quantities of raw FMC data, and only processed images are saved, which limits future data analysis. These standards are often dictated by independent regulators, such as the Office for Nuclear Regulation (ONR) in the UK.

There is a clear benefit to compressing stored data to the point where information can be as comprehensively analysed in the future as at the time of inspection, while limiting storage space. Numerous methods have been proposed to achieve this for ultrasonic inspection, such as leveraging the reciprocity of the FMC dataset to nearly halve the data required to be collected [17, 18], termed Half Matrix Capture. Other signal processing techniques such as Compressive Sensing [19] have been shown across a number of fields for data compression, and applied to ultrasonic testing data [20]. The use of sparse phased arrays [21, 22] seeks to minimise the volume of data acquired while maximising information obtained through selective element firing. This has been shown to be effective for 2-dimensional arrays [23], where both acquisition times and processed data can be large. However, this is often at the cost of image resolution and the creation of grating lobes. Other notable compression techniques include parameter extraction [24, 25] and domain transformation [26].

However, it may be the rise in popularity of phase-based imaging that lends the simplest solution to ultrasonic data compression – namely PCI imaging using the Sign Coherence Factor (SCF). As this algorithm considers only the sign of each sampled time point, rather than the phase itself, binary quantisation of data is possible. In turn data storage can be reduced to a single-bit per time-sampled point [27]. In turn, reduced hardware requirements and faster processing are possible, as well as limiting transfer rates and the volume of data required to be stored.

A further challenge observed when considering inspections using FMC acquisition is the low energy transmission relative to other phased array methods. This challenge is intensified in scattering or layered material inspection conducted in NDT applications – for example, in austenitic metal alloys [28]. Despite advantages in post-processing focusing ability, FMC acquisition can often result in low SNR for an individual time signal as only a single element is fired at any one time. This is particularly exaggerated at high element count and low pitch arrays required to provide useful focusing in post-processing. Particularly when attempting acquisition for the purpose of PCI, this can significantly hinder imaging performance as low-amplitude responses may not be distinguishable from the noise floor, reducing the accuracy of phase coherence calculations. This issue may be further exacerbated when extended to attenuating materials or inspections involving large ultrasound travel times.

Typically, increasing the dynamic range of an ultrasonic system will result in greater signal resolution, and as such there have been numerous attempts to developed methods for improving the dynamic range of ultrasound acquisition. One such method is the simple averaging of several consecutive ultrasonic signals which can increase the dynamic range by up to $3N$ dB for every 2^N averages, for an integer N. Additionally, coded excitation has been shown to improve ultrasound SNR by over 20 dB through increasing the average power of a transmitted waveform [29-31]. Despite seeing limited deployment in NDT, it has been shown that by implementing orthogonal Golay-based coded excitation, the dynamic range of TFM imaging in steel can be maintained through dry coupled media without compromise to range resolution or acquisition time [32].

It is clear that both PCI and coded excitation have individually demonstrated unique advantages when approaching advanced ultrasonic imaging techniques. However, these have not yet been implemented together. This work will show that there are a number of benefits attainable by combining these methods.

Firstly, implementing both PCI and coded excitation techniques indicates the potential for data size reduction techniques, by combining the single-bit nature of PCI with the pulse compression techniques of coded excitation. Additionally, work by Isla and Cegla [33] has previously shown that using ultrasonic phased arrays can be generated using binary receive data, demonstrating higher data rates and throughput. If stored before pulse compression, data can be stored compactly with single-bit precision, with the possibility of high frame rate and low latency imaging.

Furthermore, hardware simplification is possible, firstly due to SNR gains offered by coded excitation, allowing dynamic range to be preserved at low voltages and removing the

requirement for high-voltage pulsers. The use of Analogue-to-Digital Converters (ADCs) can be replaced by simplified hardware suitable for single-bit digitisation, such as comparators.

This work will show that through single-bit digitisation of FMC data using coded excitation, PCI images of notch tip-diffraction using phase coherence can be generated with high SNR. Additionally, it will be shown that pulse compression of the single-bit coded excitation signals provides sufficient resolution to generate amplitude TFM images with imaging performance comparable to those generated through standard single-cycle acquisition.

II. Technical Background

A. Coded Excitation

The concept of coded excitation, first discussed at Bell Labs in the early 1950s [34], sought to improve radar range and accuracy through the use of frequency modulated pulses. Application of this technology achieved transmission outputs with orders of magnitude greater energy than traditional pulses, and without any increase to input power [35]. The use of pulse modulation was later applied to medical ultrasound to improve imaging performance [36], and finally to wider ultrasonic phased array use [31]. Nowadays, coded excitation is a term given to a range of pulse compression techniques used to improve the dynamic range of received ultrasonic signals.

Stemming from increasing use within the medical diagnostic imaging field, the first use of coded excitation in NDT was to increase the sensitivity of flaw detection using immersion transducers in pitch-catch configuration [37]. Since, coded excitation has been exploited for many practical NDT applications, including air coupled ultrasonic transducers [38, 39], ultrasonic inspection of carbon fibre polymers [40] and attenuating materials [41], guided waves [42], and thermography [43]. Many modulation techniques have been presented and discussed for these applications, including chirps [44, 45], Barker and Golay [46, 47] code excitation.

Coded excitation involves the transmission of a long coded pulse, from which a coded received signal is obtained. The peak transmission power remains constant, but the average transmission power is increased with the longer pulse relative to single cycle transmissions. Using pulse compression techniques, the received signal is decoded, resulting in a higher SNR and resolution signal.

This work will focus on the use of complementary Golay series for pulse modulation [48]. Unlike the majority of pulse compression techniques, excitation using complementary Golay pairs can supresses the formation of sidelobes. These can be generated using a recursive algorithm [49], resulting in sequences of 2^N cycles, where N is an integer number. Furthermore, the ability to perform pulse compression using binary excitations can provide benefits in simplified pulse generation architecture design, contrary to other coded excitation methods which require high level pulsers.

To implement Golay excitation with an FMC acquisition, a traditional single transmission pulse is replaced with two subsequent transmissions, taking the form of each Golay pair, Tx_1 and Tx_2. The overall transmission number is therefore doubled, and in turn so too the number of received signals.

It is the similar yet inverse nature of these waveforms that together allow sidelobe suppression to be achieved. This can be demonstrated by considering the correlation of each transmission waveform with their matched filters Rx_1 and Rx_2. The autocorrelation functions obtained from each waveform can then be summed, with constructive addition of the main lobe, and cancellation of sidelobes. The result is a compressed waveform Rx_P with reduced peak sidelobe level. This process is shown visually in Fig. 1.

In reality, the received time-trace from each Golay transmission form the matched filters, and a compressed time signal Rx_P is obtained. This process is conducted for each pair collected during the FMC acquisition, resulting in a compressed dataset. The expression for processing a single pair is given in (1).

$$Rx_P = (Tx_1 * Rx_1) + (Tx_2 * Rx_2) \tag{1}$$

The SNR improvement using this method is two-fold; a 3 dB improvement is observed from the averaging of two time signals, with a further 3 dB increase for each increment of N [50]. The SNR improvement expected from an N-cycle Golay transmission is given as the expression in (2) [32].

$$\Delta SNR = 3(N+1)\ dB \tag{2}$$

Although the number of transmission events is doubled, the net acquisition time can remain unchanged by selecting mutually orthogonal Golay pairs. This allows two waveforms to be transmitted simultaneously without interference, allowing them to be separated during pulse compression [32, 47, 51].

One drawback of pulse modulation arises when considering large cycle numbers, which increases the dead zone directly after transmission. The length of this dead zone is proportional to the number of cycles used, and can prevent detection of near-source reflectors. However, in most NDT applications, immersion or acoustic wedge delay lines are used to introduce

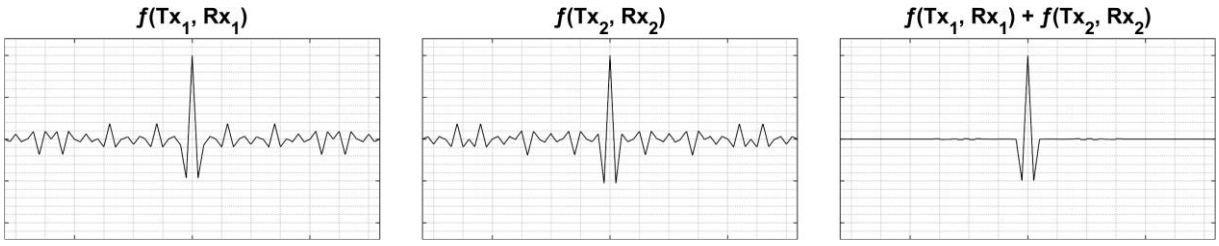

Fig. 1. Demonstration of sidelobe suppression by the sum of two complimentary Golay functions, resulting in a single main lobe

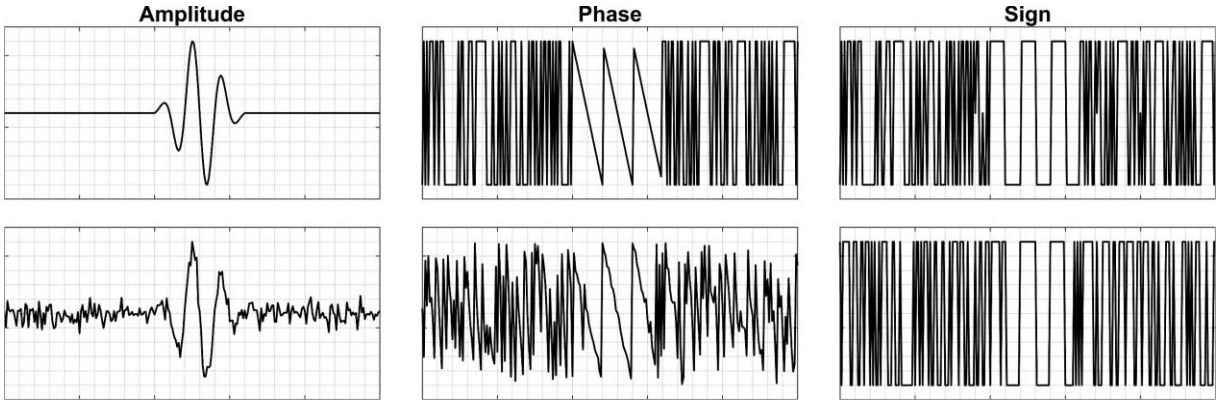

Fig. 2. From left column to right column, the amplitude, phase and sign of a Gaussian pulse with (top row) and without (bottom row) noise.

a stand-off between the array and inspected specimen. This provides an effective time delay medium such that the dead zone does not impact the desired inspection area.

B. Total Focusing Method

Unlike conventional PAUT, focusing using the TFM algorithm is not physically achieved through beamforming, but rather by applying delay laws in post processing [5]. This increases the flexibility of imaging, as beamforming is completed computationally and it not limited by time constraints of extensive focusing using physical beamforming. TFM enables full-aperture focusing of a full array at every point in a region of interest. This region is discretised into pixels, each contributing an amplitude value to the total image.

For an array with N_{tx} transmitting and N_{rx} receiving apertures, using an FMC dataset $\hat{u}$ and transmit and receive delay laws τ_{tx} and τ_{rx}, the TFM image I_{TFM} an be computed using (3), where M is the total transmit-receive events in the dataset.

$$I_{TFM} = \frac{1}{M}\sum_{tx=1}^{N_{tx}}\sum_{rx=1}^{N_{rx}} \hat{u}_{tx,rx}(\tau_{tx} + \tau_{rx}) \tag{3}$$

This imaging method is typically used in NDT fields, where beamforming is performed in both transmission and reception. In medical fields, a similar algorithm is used – the Synthetic Aperture Focusing Technique (SAFT) [52]. Unlike TFM, SAFT is focused in only reception such that a final image is generated by the summation of low-resolution images from each single-element transmission. Although not presented in this paper, the conclusions drawn from using TFM can likely be applied to SAFT imaging.

C. Phase Coherence Imaging

Contrary to traditional full matrix processing algorithms like TFM, Phase Coherence Imaging (PCI) considers only the phase of received data, rather than amplitude. There have been several methods for computation of phase coherence for ultrasonic imaging discussed throughout relevant literature [6, 12]. However, the most computationally efficient method is the use of the sign as an approximation of the phase.

The top row of Fig. 2 shows how the amplitude, phase and sign are related for a perfect Gaussian waveform. It is clear that the sign is a generalisation of the phase, essentially describing the state of the piezoelectric transducer at each sample point as either expanded (>1) or compressed (<1) from equilibrium. Therefore, despite the amplitude difference at two points of the same polarity in the wavelet, the assigned value is the same.

Now considering the same waveform with added random noise, as in the bottom row of Fig. 2, the behaviour of the phase and sign of the wavelet is unchanged. However, noise areas surrounding the wavelet have random and unstructured phase values. The basis of the PCI algorithm relies on the assumption that the phase and sign values at points of random noise will be destructive over the summation of the full matrix dataset, and tend to zero with increasing data size, while values from the coherent waveforms will constructively sum with increasing data size. Ultimately, the 'SNR' using this method is determined both by the number of individual time signals used to form the image, and the number of time signals which contain a coherent reflector signal.

The nature of the wavelet phase requires that the signal has sufficient amplitude to be distinguished from the noise floor. For signals with larger travel times, there will come a critical point where the noise dominates the wavelet and the phase and sign are no longer consistent, reducing the coherence of phase across the dataset. Therefore, the phase of a signal response should remain measurable, such that it occurs before a 'cut-off' point where the signal falls beneath the noise floor.

The binary nature of using sign is a further benefit when considering data compression. Each sample point can be sufficiently stored as a single-bit digit by conversion to sign in hardware, greatly reducing the amount of data required to be transferred and processed [27]. Calculation of the sign $s_{tx,rx}$ from a full resolution FMC dataset can be performed simply by using (4), where $\hat{u}_{tx,rx}$ is a time signal in the FMC data corresponding to transmitting element tx and receiving element rx. The algorithm for processing the sign data into a final image I_{PCI} for an M element array is then given by (5), given a ToF τ, for N_{tx} and N_{rx} transmitting and receiving elements respectively.

$$s_{tx,rx}(t) = \begin{cases} 1, & if\ \hat{u}_{tx,rx}(t) \geq 0 \\ -1, & if\ \hat{u}_{tx,rx}(t) < 0 \end{cases} \tag{4}$$

$$I_{PCI} = \left|\frac{1}{M}\sum_{tx=1}^{N_{tx}}\sum_{rx=1}^{N_{rx}} s_{tx,rx}(\tau_{tx} + \tau_{rx})\right| \tag{5}$$

Applying this process in acquisition hardware would remove the requirement of high-resolution ADCs to obtain a digital signal. Instead, these could be replaced by a simple comparator

- reducing the complexity, size and cost of necessary array controllers. Similarly to the method described above for software processing, the comparator compares an input voltage V_{In} to a reference voltage V_{Ref}. Depending on the polarity of the input relative to this reference, either a positive or negative saturation voltage V_{Sat} is applied to the output. The result is a binary signal with minimal processing which can be used for PCI imaging.

One important practical consideration for this hardware implementation is the presence of a DC offset. This can offset the polarity of single-bit data and lead to incorrect sign values. If the DC offset is larger than the noise level, the ability to determine noise by the summation of phase values is removed, as they will constructively sum to a perceived large coherence. It is therefore imperative that the DC offset is removed from the analogue signal prior to digitisation by the comparator.

III. Experimental Procedure

In order to perform and collect coded excitation data, a tri-level excitation capable phased array controller (FIToolbox® from Diagnostic Sonar Ltd., Livingston, UK [53]) was used. This allowed controlled excitation of a 5 MHz 64-element linear phased array (Olympus 5L64-A32) with a 60% fractional bandwidth.

Data acquisition using the FIToolbox® array controller was performed using a LabView [54] interface, allowing manipulation of ultrasonic controls including the excitation waveform required for coded excitation.

Received data was sampled at 50 MHz, and digitised through a 12-bit ADC. This was then interpolated to 16-bit for ease of writing to and reading from file, with single-bit digitisation performed in post-processing software. This allowed for direct comparison of conventional data bit-depth and single-bit using the same dataset, with quantisation done in software rather than hardware. This was under the assumption that quantisation in post-processing would produce the same binary signal as would be acquired through hardware quantisation.

Data processing, including pulse compression and imaging, was conducted in MATLAB (The MathWorks Ltd., Natick. Massachusetts) 2023a, and accelerated with parallel CPU and GPU processing toolkits [55-57].

The test piece used in this work was designed to simulate an inspection where the use of single-bit PCI with coded excitation could be applied. PCI has been shown to increase detection and sizing capabilities of crack-tip diffraction [12], and so imaging of tip diffraction was determined to be a suitable benchmark to test this work. Furthermore, to ensure that dead zones associated with Golay transmission did not inadvertently hinder imaging at higher cycle numbers, the defect should be placed sufficiently far from the array position.

A 5.0 x 1.0 mm notch was placed in a 125.0 x 500.0 x 300.0 mm 1018 steel block, in order to mimic a planar defect. This was positioned 27.5 mm from the backwall, relative to the centre of the notch. The array was placed at a horizontal offset of 55.0 mm from the centre of the notch, as shown in Fig. 3. Data from both standard single-cycle excitation, as well as Golay excitation utilising 2 to 128 cycles were acquired through an FMC acquisition process.

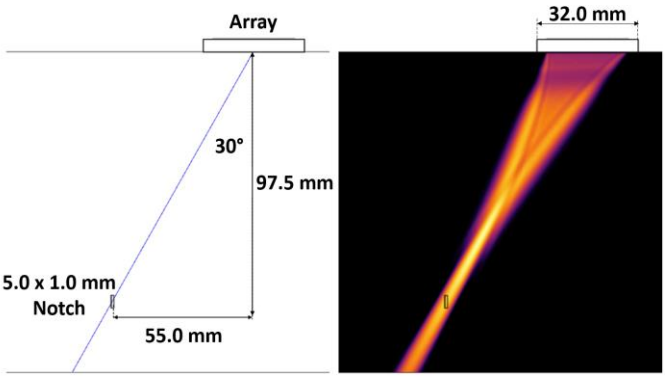

Fig. 3. Experimental setup for data collection, showing the offset of a phased array probe from a rectangular notch (left) and beam profile when the full aperture is focused at the notch centre (right)

IV. Pulse Compression

The Golay excitation waveform can be transmitted in a number of formats. Typical transmission is conducted by tri-level systems, which allows the transmission of pulses with a positive or negative polarity of 1, and zero. By considering a pulse width of 100% of the wavelength, such that a perfectly square pulse is considered, a single-bit transmission can be defined in single-bit format.

As previously mentioned, data was digitised using a 12-bit ADC and stretched through interpolation to 16-bit for the purposes of saving the data to file. This was quantised digitally in post-processing software to obtain the single-bit format. As discussed, this is also possible to do with hardware alone, by digitising using a simple comparator as a single-bit ADC.

Once FMC data is acquired using Golay excitation, each element-pair is associated with two receive signals Rx_1 and Rx_2. Both the uncompressed and compressed receive data for a single element-pair is shown in Fig. 4, using both 12-bit and single-bit data. The compressed signal generated from the single-bit receiver quantisation retains much of the amplitude information seen in the 12-bit compressed signal, however it exhibits a longer dead zone. This is caused by the amplification of the element 'ringdown' during quantisation, and remains consistent until reaching the noise floor. For this reason, the bandwidth and dampening properties of the array are important to determine the size of this dead zone extension, regardless of Golay cycle number.

The single-bit correlation function measures the correlation in the phase of the excitation pulse and its received signal at each cycle in the transmission. High amplitude is seen when there is a strong phase match between the transmission cycles and reception, with low amplitude when there is little phase correlation, e.g. at points containing incoherent noise.

V. Compression SNR Analysis

In order to understand the effect of quantising received data prior to pulse compression, the top tip diffraction response from the EDM notch was studied. SNR was calculated by considering the maximum response from the backwall signal, with the noise calculated using the root-mean square. The noise region was considered from the point at which ring-down of the

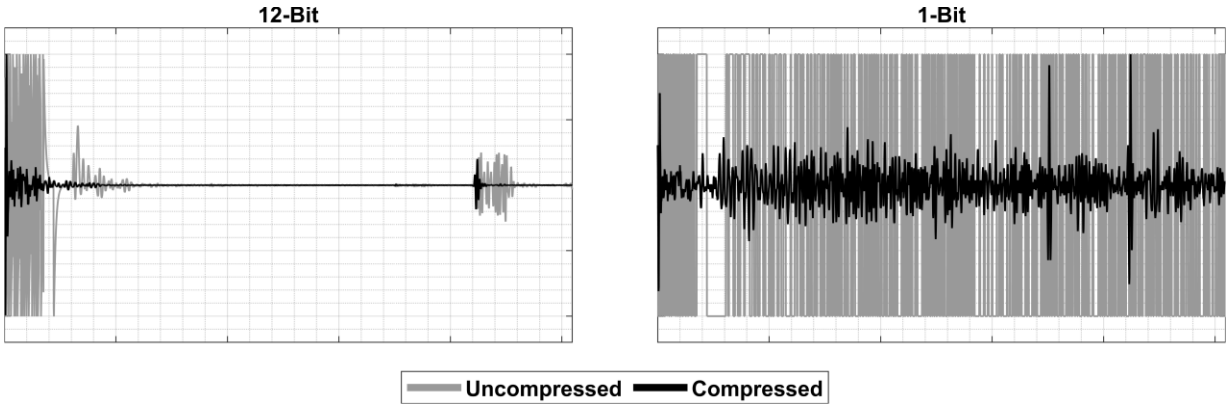

Fig. 4. Demonstration of pulse compression using 12-bit (left) and single-bit (right) receiver quantisation and receive signals. The raw signal is shown in grey, with the resulting compressed A-Scan highlighted in black.

transducer had reached the noise floor, to before the backwall indication.

For the 12-bit receiver quantisation, the resulting SNR of this response was 18.0 dB, with the single-bit receiver quantisation data producing 14.5 dB SNR. This reduction is expected, as the data bit-depth is massively reduced.

However, this suggests that despite a significant reduction in bit-depth of input data, from 2^{12} to 2^{1}, a large amount of data is retained and exploited during pulse compression – with unexpectedly low impact on processed time signal SNR. It appears that although the input received signal is binary in nature, data is still maintained across the pulse length. It can be theorised that increasing the number of cycles in transmission will increase the bit-depth of the processed data.

This study was expanded by observing the SNR of the backwall response for varying numbers of Golay excitation cycles, using both 12-bit and single-bit inputs. Transmissions of Golay cycles from 2 to 128 were used, with a duty cycle of 100%, the results of which are graphically shown in Fig. 5.

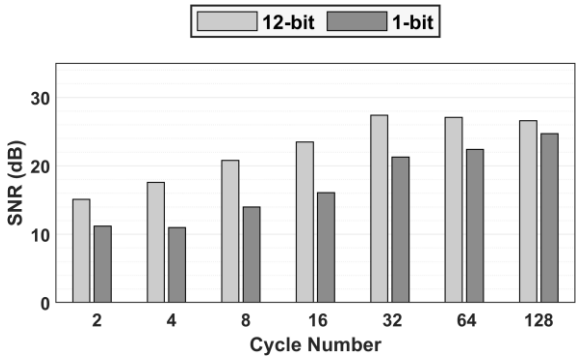

Fig. 5. SNR Analysis of backwall indication utilising 12-bit and 1-bit receiver quantisation data with 100% duty cycle

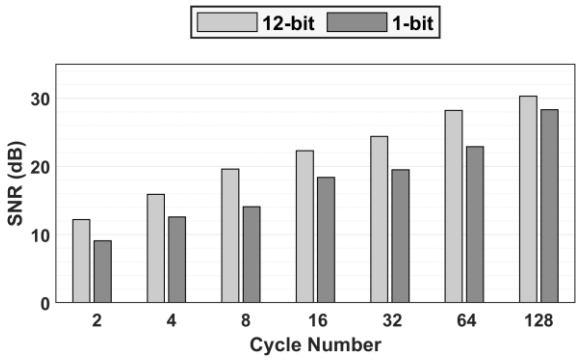

Fig. 6. SNR Analysis of backwall indication utilising 12-bit and 1-bit receiver quantisation data with 71% duty cycle

Theoretically, it is expected that with each doubling of cycle number, there should be a 3 dB increase in SNR. This is explained by the root-sum square nature of the summation of two noise signals, which leads to a $\sqrt{2}$ reduction in noise and translates to a 3 dB SNR increase.

The 12-bit receiver quantisation data follows this 3 dB trend up to and including the use of 32 cycles, after which the SNR plateaus. Interestingly, the single-bit receiver quantisation data does not follow this trend. Despite showing little SNR improvement at low cycle numbers, the SNR continues to rise with increasing cycle number.

The plateau of this trend is likely due to an asymmetry between positive and negative transmission cycles of the complimentary Golay pair. Any asymmetry between positive and negative excitation pulses will lead to imperfect compression, and therefore reduced performance in the cancellation of sidelobes. It has been shown that this asymmetry can occur from the finite time required for the pulser to change the transmission polarity, termed 'rise time'. These non-zero rise times are particularly applicable when considering square pulses considered in this case [58]. It should be noted that pulse compression degradation of Golay code has also been attributed to the generation of noise due to inadequate quantisation of received signals [59], signal aliasing and doppler effects of large scanning speeds [58], as well as nonlinearities [60], which should not impact pulse compression integrity in this work.

It is likely that once the SNR is sufficiently high, this degradation begins to dominate the noise level and prevents further SNR improvement. However, when considering compression using single-bit inputs, only asymmetric polarity is considered, which has less of an effect on compression degradation as the square wave is more closely preserved in reception. Therefore, the SNR continues to improve with increasing cycle numbers.

Considering the same study, instead with a 71% duty cycle, we observe the trend seen in Fig. 6. The SNR no longer plateaus at higher cycle frequencies for the 12-bit receiver quantisation, and the 3 dB SNR increase is approximately observed. There is a mean 4.0 dB difference in SNR value between the 12-bit and single-bit receiver quantisation across this trend. This improvement is due to the sine-like behaviour of the

transmission signal. The 100% duty cycle assumes the pulser switches polarity across a single sample point. This is not the case and therefore leads to a breakdown during pulse compression. The 71% duty cycle attempts to align with the natural cycle of the pulser, and follows the desired input signal resulting in lesser pulse compression breakdown.

Furthermore, the pulser may not be able to provide a consistent voltage at high cycle numbers, with the power depleting over the pulse time. The 'on' time of the pulser for the 100% duty cycle is greater, and therefore this effect may be of higher significance and impact lower cycle numbers than that of the 71% cycle.

Despite the loss of SNR when considering a single-bit receiver quantisation, a notable benefit is obtained through the reduction in data size. The use of Golay coded excitation doubles the data size due to the double firing requirement, however, there is a factor of 12 reduction in memory usage when compressing data at single-bit from 12-bit. This suggests that processing and streaming data would improve in efficiency by a similar factor. Particularly when considering the large number of frames acquired during component scanning, the memory saved by using single-bit data is sizeable.

There is therefore a trade-off when approaching these methods. Reduced data sizes and processing times associated with single-bit acquisition introduces an SNR reduction. However, for inspection cases where this approximate 4 dB reduction is acceptable, single-bit acquisition is preferable.

It should be noted that this study was conducted using FMC data, and therefore single-element firing. As such, the backwall indication is contained well within the dynamic range of the 12-bit ADC and just above the noise floor. This was done in order to ascertain the behaviour of coded excitation and single-bit digitisation techniques for this imaging case.

VI. Imaging

A. PCI Imaging

After pulse compression, the sign can be calculated and a PCI image processed as previously discussed. It should be clarified that due to the nature of the PCI algorithm, all PCI images can be considered as 'single-bit', as only the polarity is used for generation.

In order to determine the effectiveness of imaging using single-bit Golay processing, a standard single cycle dataset is used as a benchmarking reference. The single cycle data was acquired with a transmission voltage of 80 V and 48 dB of gain in reception, such that the first backwall signal was unsaturated and fully contained within the dynamic range.

A PCI image of the same 5.0 x 1.0 mm notch from sample specified in Fig. 3 formed from this data is shown on the left of Fig. 7 from a single cycle transmission dataset. As is the case with all PCI images, the image is normalised to the maximum possible coherence, which in the case of a 64-element FMC dataset is 64^2 or 4096. Both the top and bottom tip diffraction indications are clearly seen, and demonstrates the ability of PCI to resolve diffuse reflectors. Sizing the notch from this image using the maximum value from each tip provides an accurate measurement of the extent of the notch in the depth axis.

Now considering data obtained from a 16-cycle Golay transmission, a comparison between images generated using 12-bit and 1-bit pulse compression can be made. Again, acquisition was performed with an 80 V excitation and 48 dB gain. Fig. 7 contains two PCI images, formed from a 12-bit (middle) and 1-bit (right) receiver quantisation respectively. The 12-bit receiver quantisation shows similar quality to the single cycle dataset, with both top and bottom tip diffraction well resolved, and the ability to size accurately. The 1-bit receiver quantisation resolves the top tip well, however the bottom tip is not as prominent.

B. TFM Imaging

Due to signal resolution recovered during pulse compression of binary inputs, it may be possible to perform amplitude-based imaging using TFM. Firstly, a reference TFM image can be formed from the single cycle dataset, and is shown on the left of Fig. 8. The noise measurement for SNR calculation was based upon the top-right area of each image, such that no notch or backwall indication was considered. The signal was measured to be the maximum value of the top-tip indication of the notch.

The image is linearly normalised to the top-tip indication amplitude, which has an SNR of 35.7 dB. The diffraction indication from the bottom tip of the notch is much lower in amplitude than the top, at around 9% relative amplitude.

Now considering the 16-cycle Golay transmission data, with both 12- and 1-bit compression inputs, we can resolve the TFM images observed in Fig. 8. The 12-bit receiver quantisation image shows similar image quality, with a bottom tip relative amplitude drop of ~93%. However, the TFM image observed from the single-bit receiver quantisation also shows similar quality. This shows that with despite two single-bit inputs, information stored within the received signal's sign can produce a sufficient resolution signal after pulse compression to image based on amplitude. The relative amplitude of the bottom tip in this image is 5.8%, not significantly less than the 12-bit receiver quantisation.

The 12-bit input image exhibits an SNR of 39.5 dB, with the 1-bit input exhibiting a slightly lower SNR of 37.5 dB. It should also be noted that the 12-bit image contains reflections from the backwall in the bottom-left of the image. These are absent in the single-bit image, however this is likely due to the reduced sampling resolution, rather than an imaging improvement.

Given that these images were produced from the same raw dataset, no coupling or orientation variations can be contributed to the SNR difference. Therefore, the binary quantisation is the only parameter in the imaging process that could enact this change.

C. Low Voltage Excitation

The benefit of coded excitation in this case is the observed increase in dynamic range. It follows that a reduction in the transmission voltage should be possible without a dramatic reduction in SNR. Theoretically, for each halving of the input energy, an equivalent gain increase of 6 dB can be applied to counteract the energy drop, such that utilisation of the dynamic

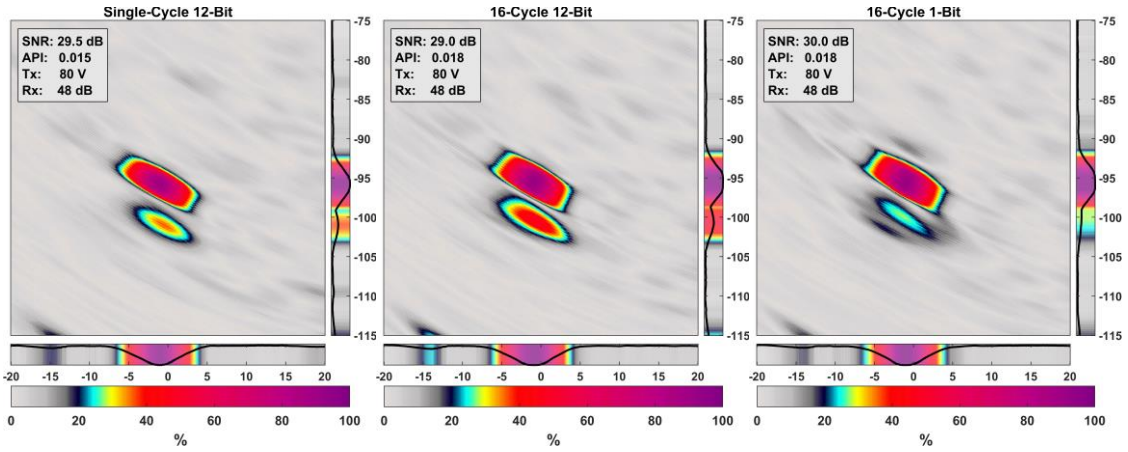

Fig. 7. PCI images processed from single cycle and 16-cycle Golay FMC datasets with 80 V excitation and 48 dB gain. Images from single-cycle data (left), 16-cycle 12-bit data (middle) and 16-cycle 1-bit data (right) are shown. The SNR, API, Tx voltage and Rx gain are presented for each image.

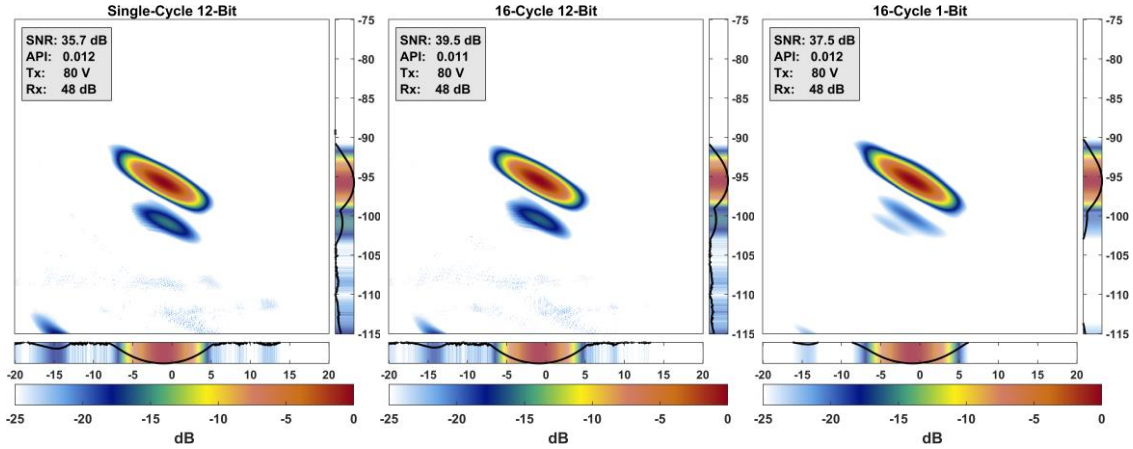

Fig. 8. TFM images processed from single cycle and 16-cycle Golay FMC datasets with 80 V excitation and 48 dB gain. Images from single-cycle data (left), 16-cycle 12-bit data (middle) and 16-cycle 1-bit data (right) are shown. The SNR, API, Tx voltage and Rx gain are presented for each image.

range remains constant in the raw time signals. Therefore, a reduction in excitation voltage to 10 V from 80 V would require a gain of 66 dB to be applied. A dataset was acquired to this effect to observe the low voltage effects of single-bit pulse compression on PCI imaging.

Fig. 9 shows the 12-bit and 1-bit receiver quantisation PCI images at low voltage excitation. The 12-bit image demonstrates a performance similar to the equivalent 80 V image, with both top and bottom tip diffraction resolved to within 12 dB of the maximum coherence value. Again, however, the single bit image fails to resolve the bottom tip to the same coherence, despite a clear top tip diffraction signal.

The drop in coherence of the bottom tip indication in the 1-bit receiver quantisation PCI image is likely due to the drop of the signal beneath the noise floor across a critical number of time signals within the FMC dataset. As discussed earlier, this results in the phase (or sign) of the indication becoming lost to the noise.

In order to quantify these results, the SNR value of the top tip was measured in each PCI image, and presented in visually in Fig. 11 (top), and numerically in Table I. Images produced through coded excitation exhibit slightly lower coherence overall, relative to the single cycle data. However, when comparing low input voltages to higher initial values, coded excitation exhibits little change in SNR for the 1-bit receiver quantisation. The independence of gain selection on saturation means that low-amplitude signals can be resolved from the noise floor and their coherence preserved at low voltages.

Additionally, the Array Performance Indicator (API) [5] quantifies the imaging performance based on the ability to resolve a point scatterer. A low API value indicates that the indication approaches a single point, while a larger API indicates spreading of the scatterer response. The dimensionless indicator considers both the wavelength of ultrasound in the medium λ, and the area A_{-6dB} at which the point scatterer response is greater than -6dB. The relationship is shown in (6).

$$API = \frac{A_{-6dB}}{\lambda^2} \tag{6}$$

This allows quantification of the imaging performance across both arrays and imaging algorithms, and relays the ability of the system to resolve a point scatterer, such as a tip diffraction indication from a notch. As observed in Table I, the API is largely unaffected by input bit-depth, excitation voltage or gain when imaging using the PCI algorithm.

The same analysis can be applied to TFM imaging. Fig. 10 shows the TFM images produced from the 12- and 1-bit

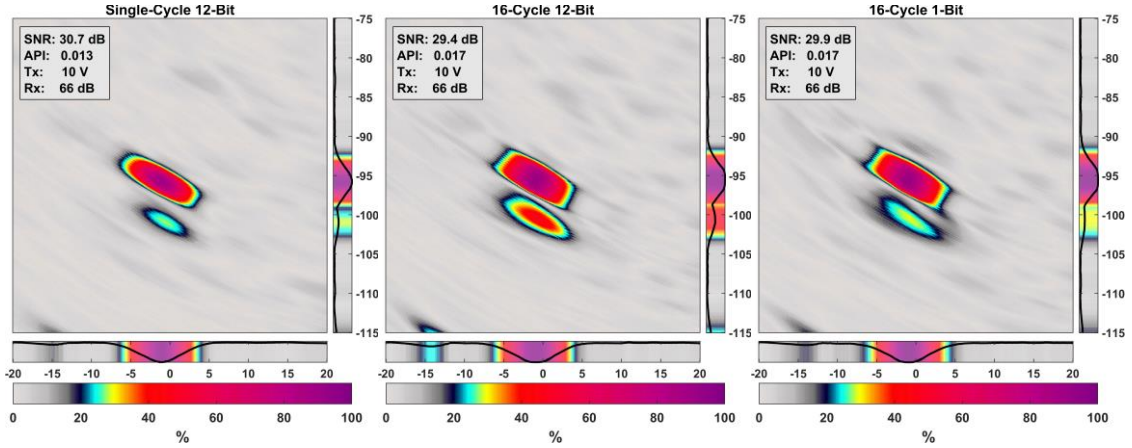

Fig. 9. PCI images processed from single cycle and 16-cycle Golay FMC datasets with 10 V excitation and 66 dB gain. Images from single-cycle data (left), 16-cycle 12-bit data (middle) and 16-cycle 1-bit data (right) are shown. The SNR, API, Tx voltage and Rx gain are presented for each image.

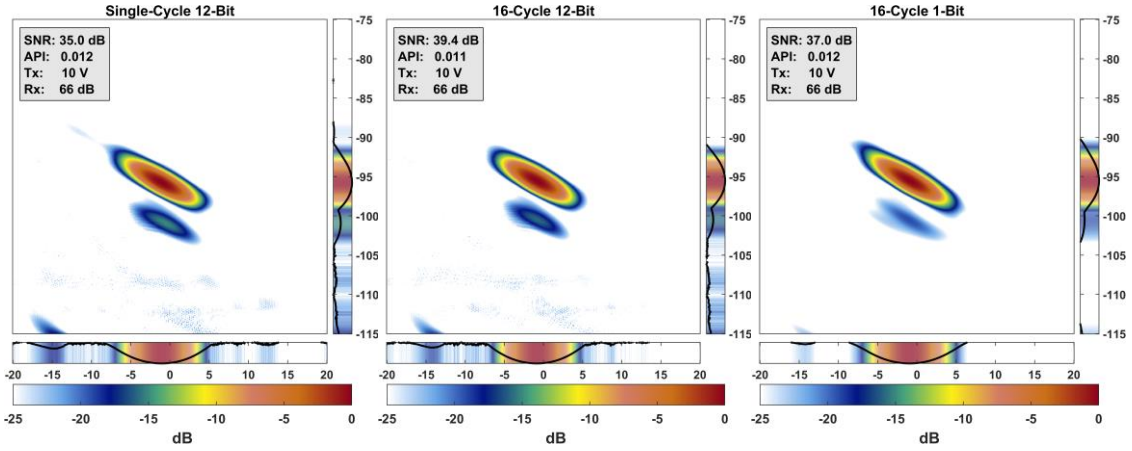

Fig. 10. TFM images processed from single cycle and 16-cycle Golay FMC datasets with 10 V excitation and 66 dB gain. Images from single-cycle data (left), 16-cycle 12-bit data (middle) and 16-cycle 1-bit data (right) are shown. The SNR, API, Tx voltage and Rx gain are presented for each image.

receiver quantisation data for a 10 V excitation with 66 dB gain. There is little impact observed on both the relative amplitude and the SNR when comparing these images to their 80 V excitation equivalents. The 1-bit image exhibits the slightly lower SNR of 37.0 dB, with a slight reduction in the bottom tip relative amplitude. The 1-bit receiver quantisation also has a slight drop in relative amplitude of the bottom tip. However, it exhibits a similar SNR value to the 80 V equivalent.

Again, the imaging performance can be quantified and is demonstrated in both Fig. 11 (bottom) and Table I. It is clear that the 1-bit receiver quantisation images exhibit a close resemblance to the 12-bit receiver quantisation. Similarly to PCI imaging, the API remains unaffected by the TFM algorithm across each dataset. It is interesting to note that the TFM algorithm out-performs the PCI in this regard, with a consistently better API value. It is clear that the 12-bit receiver quantisation images SNR remains fairly consistent, with the 1-bit receiver quantisation SNR remaining higher, with a noticeable drop at low voltage and high gain.

VII. Conclusion

This work has shown that the use of single-bit receive data for Golay coded excitation has enabled a new and efficient imaging system for data transfer, processing and storage, with little compromise to image quality. This has been demonstrated for both PCI and TFM algorithms through the use of FMC acquisition. The outcome of this work provides benefits in three key areas:

- Data compression
- Data transfer and processing rates
- Hardware complexity

The compression by use of single-bit receive data can prove beneficial across a number of industrial applications where regulations dictate the storage of historical data over several decades. This would reduce the volume of storage infrastructure required, limiting costs and space. Consequently, data accessibility is more efficient with a greater density of data accessible with the same read speeds. Energy efficiency is also improved with fewer physical storage devices to manage.

In addition to the obvious compression benefits, improved imaging frame rates could be achieved by acceleration of pulse compression and imaging processing. The ability to recover a high resolution received signal from two single-bit inputs allows both PCI and TFM imaging to be performed. Currently, commercial use of TFM is hindered by limited frame rates and costly hardware acceleration required for real-time imaging

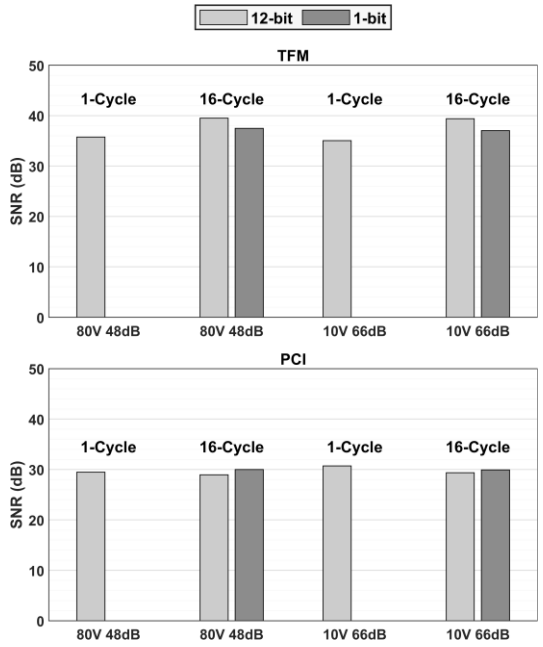

Fig. 11. SNR Analysis of notch indication in TFM image utilising 12-bit and 1-bit receiver quantisation. This is demonstrated for TFM (top) and PCI(bottom) for both high and low input voltages.

TABLE I
QUANTITATIVE PERFORMANCE OF PCI & TFM IMAGING

	Single Cycle		16-Cycle Golay			
Resolution	**12-Bit**		**12-Bit**		**1-Bit**	
Tx (V)	80	10	80	10	80	10
Rx (dB)	48	66	48	66	48	66
PCI SNR	29.5	30.7	29.0	29.4	30.0	29.9
PCI API	0.015	0.013	0.018	0.017	0.018	0.017
TFM SNR	35.7	35.0	39.5	39.4	37.5	37.0
TFM API	0.011	0.012	0.011	0.011	0.012	0.012

such as GPUs [61] and FPGAs [62]. However, this lightweight method using coded excitation could improve transfer and processing times and allow for a wider practical field of view. In addition, fast transfer and processing rates can enhance the sensor-based communication and automation propelled by NDE 4.0 [63].

The third benefit is the savings gained on hardware requirements. High voltage circuitry typically requires larger areas and are more discrete, increasing the hardware volume required relative to standard integrated Circuits (ICs). Additionally, this results in complex hardware requiring localised cooling and high voltage power supplies. By ensuring that transmission and reception operate within the same low voltage range with coded excitation, both the transmission and reception can be handled by the same IC, reducing complexity, board size and power consumption. Furthermore, low-voltage excitation enables the design of an "intrinsically safe" array controller, which could operate in otherwise unsafe conditions for current array controllers. Further benefits of a low voltage system include improvements to battery and array life, and lesser piezoelectric stresses - prolonging probe lifespan. Additionally, replacing the need for ADCs with simple comparators reduces both the hardware complexity and size. This further increases power efficiency, while reducing latency associated with digitising data with ADCs.

The combination of these factors can provide the foundation for a handheld and intrinsically safe ultrasonic acquisition and imaging system, with manageable power consumption and battery life. The ability to perform high-quality imaging in challenging environments with a lightweight system could prove invaluable across many fields. Examples of this could include use in medical theatres for tissue monitoring during operation, or by emergency medical services for on-site use. Industrially, applications can range from use in damp conditions experienced in offshore oil and gas inspection, or in renewable energy fields where a handheld device could improve inspection practicality.

However, there are also a number of limitations associated with this work, the most obvious of which is the reduced resolution of stored data. This imposes a restriction on the scope of future data analysis outside the image generation outlined in this work. Furthermore, the use of coded excitation and necessary pulse compression introduces an additional step in the processing of data that must be considered when approaching real-time applications.

This work also assumes that an indication is distinguishable from noise. If this is not the case, such as in attenuating materials or when considering large travel paths, single-bit pulse compression may not be beneficial, particularly at low transmit voltages. Furthermore, a single imaging scenario is presented in this work, highlighting the imaging of tip diffraction from a rectangular notch. Future work in this area must consider multiple imaging scenarios, including probe positioning, reflector type, the inclusion of delay lines, and attenuating media.

Future work to further explore a single-bit PCI and TFM imaging platform using coded excitation would require the design of an array controller with the capability to perform quantisation in-hardware. This would allow complications such as DC offsets and transfer rate improvements to be explored fully.

ACKNOWLEDGMENT

This work is supported by EPSRC Centre for Doctoral Training in Future Innovation in Non-Destructive evaluation (FIND) under EPSRC Grant No. EP/S023275/1.

REFERENCES

[1] W. Gebhardt, *Improvement of Ultrasonic Testing by Phased Arrays*. Nuclear Engineering and Design, 1983. **76**(3): p. 275-283.

[2] B. W. Drinkwater and P. D. Wilcox, *Ultrasonic Arrays for Non-Destructive Evaluation: A Review*. NDT & E International, 2006. **39**(7): p. 525-541.

[3] Z. Jie, et al., *Comparison of Ultrasonic Array Imaging Algorithms for Nondestructive Evaluation*. IEEE Transactions on Ultrasonics, Ferroelectrics, and Frequency Control, 2013. **60**(8): p. 1732-1745.

[4] C. Holmes, et al., *The Post-Processing of Ultrasonic Array Data Using the Total Focusing Method*. Insight - Non-Destructive Testing and Condition Monitoring, 2004. **46**(11): p. 677-680.

[5] C. Holmes, et al., *Post-Processing of the Full Matrix of Ultrasonic Transmit–Receive Array Data for Non-Destructive Evaluation*. NDT & E International, 2005. **38**(8): p. 701-711.

[6] J. Camacho, et al., *Phase Coherence Imaging*. IEEE Transactions on Ultrasonics, Ferroelectrics and Frequency Control, 2009. **56**(5): p. 958-974.

[7] N. Portzgen, et al., *Inverse Wave Field Extrapolation: A Different Ndi Approach to Imaging Defects*. IEEE Transactions on Ultrasonics, Ferroelectrics and Frequency Control, 2007. **54**(1): p. 118-127.

[8] A. J. Hunter, et al., *The Wavenumber Algorithm for Full-Matrix Imaging Using an Ultrasonic Array*. IEEE Transactions on Ultrasonics, Ferroelectrics and Frequency Control, 2008. **55**(11): p. 2450-2462.

[9] J. Zhang, et al., *Defect Detection Using Ultrasonic Arrays: The Multi-Mode Total Focusing Method*. NDT & E International, 2010. **43**(2): p. 123-133.

[10] P. D. Wilcox, et al., *Advanced Reflector Characterization with Ultrasonic Phased Arrays in Nde Applications*. IEEE Transactions on Ultrasonics, Ferroelectrics, and Frequency Control, 2007. **54**(8): p. 1541-1550.

[11] J. F. Cruza, et al., *Plane-Wave Phase-Coherence Imaging for Nde*. NDT & E International, 2017. **87**: p. 31-37.

[12] J. Camacho, et al., *Ultrasonic Crack Evaluation by Phase Coherence Processing and Tfm and Its Application to Online Monitoring in Fatigue Tests*. NDT & E International, 2018. **93**: p. 164-174.

[13] B. Gauthier, et al., *Towards an Alternative to Time of Flight Diffraction Using Instantaneous Phase Coherence Imaging for Characterization of Crack-Like Defects*. Sensors, 2021. **21**(3): p. 730.

[14] Y. Javadi, et al., *Continuous Monitoring of an Intentionally-Manufactured Crack Using an Automated Welding and in-Process Inspection System*. Materials & Design, 2020. **191**: p. 108655.

[15] Y. Javadi, et al., *High-Temperature in-Process Inspection Followed by 96-H Robotic Inspection of Intentionally Manufactured Hydrogen Crack in Multi-Pass Robotic Welding*. International Journal of Pressure Vessels and Piping, 2021. **189**: p. 104288.

[16] D. G. Aggelis and A. S. Paipetis, *Monitoring of Resin Curing and Hardening by Ultrasound*. Construction and Building Materials, 2012. **26**(1): p. 755-760.

[17] C. Holmes, et al., *Advanced Post-Processing for Scanned Ultrasonic Arrays: Application to Defect Detection and Classification in Non-Destructive Evaluation*. Ultrasonics, 2008. **48**(6-7): p. 636-642.

[18] D. Lines, *Rapid Distributed Data Collection with Arrays - the Next Step Beyond Full Waveform Capture*. Insight, 2006. **48**.

[19] M. Fornasier and H. Rauhut, *Compressive Sensing*. 2011, Springer New York. p. 187-228.

[20] Z. Bai, et al., *Compressive Sensing of Phased Array Ultrasonic Signal in Defect Detection: Simulation Study and Experimental Verification*. Structural Health Monitoring, 2018. **17**(3): p. 434-449.

[21] P. Yang, et al., *A Novel Method to Design Sparse Linear Arrays for Ultrasonic Phased Array*. Ultrasonics, 2006. **44**: p. e717-e721.

[22] L. Moreau, et al., *Ultrasonic Imaging Algorithms with Limited Transmission Cycles for Rapid Nondestructive Evaluation*. IEEE Transactions on Ultrasonics, Ferroelectrics, and Frequency Control, 2009. **56**(9): p. 1932-1944.

[23] A. Austeng and S. Holm, *Sparse 2-D Arrays for 3-D Phased Array Imaging - Design Methods*. IEEE Transactions on Ultrasonics, Ferroelectrics, and Frequency Control, 2002. **49**(8): p. 1073-1086.

[24] Y. Lu, et al., *A Successive Parameter Estimation Algorithm for Chirplet Signal Decomposition*. IEEE Transactions on Ultrasonics, Ferroelectrics and Frequency Control, 2006. **53**(11): p. 2121-2131.

[25] Y. Nabil, et al. *Ultrasonic Signals Parameters Estimation Based on Differential Evolution*. in *3rd International Conference on Control Engineering & Information Technology (CEIT)*. 2015. IEEE.

[26] G. Cardoso and J. Saniie. *Performance Evaluation of Dwt, Dct, and Wht for Compression of Ultrasonic Signals*. in *IEEE Ultrasonics Symposium, 2004*. 2004.

[27] B. Gauthier, et al., *Lightweight and Amplitude-Free Ultrasonic Imaging Using Single-Bit Digitization and Instantaneous Phase Coherence*. IEEE Transactions on Ultrasonics, Ferroelectrics, and Frequency Control, 2022. **69**(5): p. 1763-1774.

[28] L. J. Cunningham, et al., *The Detection of Flaws in Austenitic Welds Using the Decomposition of the Time-Reversal Operator*. Proceedings of the Royal Society A: Mathematical, Physical and Engineering Sciences, 2016. **472**(2188): p. 20150500.

[29] R. Y. Chiao and H. Xiaohui, *Coded Excitation for Diagnostic Ultrasound: A System Developer's Perspective*. IEEE Transactions on Ultrasonics, Ferroelectrics, and Frequency Control, 2005. **52**(2): p. 160-170.

[30] S. Zhou, et al. *Medical High-Frequency Ultrasound Imaging Using Golay-Coded Pulse Excitation*. in *2012 5th International Conference on BioMedical Engineering and Informatics*. 2012.

[31] M. O'Donnell, *Coded Excitation System for Improving the Penetration of Real-Time Phased-Array Imaging Systems*. IEEE Transactions on Ultrasonics, Ferroelectrics and Frequency Control, 1992. **39**(3): p. 341-351.

[32] D. Lines, et al. *Using Coded Excitation to Maintain Signal to Noise for Fmc+Tfm on Attenuating Materials*. in *IEEE International Ultrasonics Symposium*. 2019. IEEE.

[33] J. A. Isla and F. B. Cegla, *Simultaneous Transmission and Reception On all Elements of an Array: Binary Code Excitation*. Proceedings of the Royal Society A: Mathematical, Physical and Engineering Sciences, 2019. **475**(2225): p. 20180831.

[34] C. E. Cooke, *The Early History of Pulse Compression Radar-the History of Pulse Compression at Sperry Gyroscope Company*. IEEE Transactions on

Aerospace and Electronic Systems, 1988. **24**(6): p. 825-833.
[35] J.R. Klauder, et al., *The Theory and Design of Chirp Radars*. Bell Labs Technical Journal, 1960. **39**(4).
[36] Y. Takeuchi, *An Investigation of a Spread Energy Method for Medical Ultrasound Systems: Part One: Theory and Investigation*. Ultrasonics, 1979. **17**(4): p. 175-182.
[37] F. Lam and J. Szilard, *Pulse Compression Techniques in Ultrasonic Non-Destructive Testing*. Ultrasonics, 1976. **14**(3): p. 111-114.
[38] T. H. Gan, et al., *The Use of Broadband Acoustic Transducers and Pulse-Compression Techniques for Air-Coupled Ultrasonic Imaging*. Ultrasonics, 2001. **39**(3): p. 181-194.
[39] D. Hutchins, et al., *Coded Waveforms for Optimised Air-Coupled Ultrasonic Nondestructive Evaluation*. Ultrasonics, 2014. **54**(7): p. 1745-1759.
[40] M. K. Rizwan, et al., *Ultrasonic Imaging of Thick Carbon Fiber Reinforced Polymers through Pulse-Compression-Based Phased Array*. Applied Sciences, 2021. **11**(4): p. 1508.
[41] D. A. Hutchins, et al., *Ultrasonic Propagation in Highly Attenuating Insulation Materials*. Sensors, 2020. **20**(8): p. 2285.
[42] J. Lin, et al., *Excitation Waveform Design for Lamb Wave Pulse Compression*. IEEE Transactions on Ultrasonics, Ferroelectrics, and Frequency Control, 2016. **63**(1): p. 165-177.
[43] H. Malekmohammadi, et al., *Comparison of Optimisation Strategies for the Improvement of Depth Detection Capability of Pulse-Compression Thermography*. Quantitative InfraRed Thermography Journal, 2020. **17**(1): p. 26-39.
[44] M. Pollakowski and H. Ermert, *Chirp Signal Matching and Signal Power Optimization in Pulse-Echo Mode Ultrasonic Nondestructive Testing*. IEEE Transactions on Ultrasonics, Ferroelectrics and Frequency Control, 1994. **41**(5): p. 655-659.
[45] J. Mamou, et al., *Chirp-Coded Excitation Imaging with a High-Frequency Ultrasound Annular Array*. IEEE Trans Ultrason Ferroelectr Freq Control, 2008. **55**(2): p. 508-13.
[46] Z. Fan, et al., *Convolution of Barker and Golay Codes for Low Voltage Ultrasonic Testing*. Technologies, 2019. **7**(4): p. 72.
[47] I. Trots, *Mutually Orthogonal Golay Complementary Sequences in Synthetic Aperture Imaging Systems*. Archives of Acoustics, 2015. **40**(2): p. 283-289.
[48] M. Golay, *Complementary Series*. IRE Transactions on Information Theory, 1961. **7**(2): p. 82-87.
[49] X. Huang. *Complementary Properties of Hadamard Matrices*. 2006. IEEE.
[50] O. Siljama, et al., *Automated Flaw Detection in Multi-Channel Phased Array Ultrasonic Data Using Machine Learning*. Journal of Nondestructive Evaluation, 2021. **40**(3).
[51] F. Zhao and J. Luo, *Diverging Wave Compounding with Spatio-Temporal Encoding Using Orthogonal Golay Pairs for High Frame Rate Imaging*. Ultrasonics, 2018. **89**: p. 155-165.
[52] J. A. Jensen, et al., *Synthetic Aperture Ultrasound Imaging*. Ultrasonics, 2006. **44**: p. e5-e15.
[53] D. I. A. Lines, et al., *Real-Time Full Matrix Capture + Total Focusing and Other Novel Imaging Options Using General Purpose Pc-Based Array Instrumentation*. Insight - Non-Destructive Testing and Condition Monitoring, 2012. **54**(2): p. 86-90.
[54] National Instruments, *Labview V17 (64-Bit)*. 2017.
[55] MathWorks, *Matlab*. 2022.
[56] MathWorks, *Gpu Coder*. 2022.
[57] MathWorks, *Parrallel Computing Toolbox*. 2022.
[58] P. Jeong, et al., *Performance Evaluation of the Golay Code Pulse Compression Technique*. Research in Nondestructive Evaluation, 1996. **8**(3): p. 125-147.
[59] G. Hayward and Y. Gorfu, *A Digital Hardware Correlation System for Fast Ultrasonic Data Acquisition in Peak Power Limited Applications*. IEEE Transactions on Ultrasonics, Ferroelectrics and Frequency Control, 1988. **35**(6): p. 800-808.
[60] F. Hamilton, et al., *Nonlinear Harmonic Distortion of Complementary Golay Codes*. Ultrasonic Imaging, 2023. **45**(1): p. 22-29.
[61] M. Sutcliffe, et al., *Real-Time Full Matrix Capture for Ultrasonic Non-Destructive Testing with Acceleration of Post-Processing through Graphic Hardware*. NDT & E International, 2012. **51**: p. 16-23.
[62] M. Njiki, et al. *A Multi-Fpga Implementation of Real-Time Reconstruction Using Total Focusing Method*. in *2013 IEEE International Conference on Cyber Technology in Automation, Control and Intelligent Systems*. 2013.
[63] J. Vrana, et al., *Handbook of Nondestructive Evaluation 4.0*. 2022: Springer International Publishing.